LAWRENCE
LIVERMORE
NATIONAL
LABORATORY

LLNL-JRNL-650395

The ion-ion hybrid Alfvén resonator in a fusion environment

W. A. Farmer, G. J. Morales

February 24, 2014

Physics of Plasmas

Disclaimer

This document was prepared as an account of work sponsored by an agency of the United States government. Neither the United States government nor Lawrence Livermore National Security, LLC, nor any of their employees makes any warranty, expressed or implied, or assumes any legal liability or responsibility for the accuracy, completeness, or usefulness of any information, apparatus, product, or process disclosed, or represents that its use would not infringe privately owned rights. Reference herein to any specific commercial product, process, or service by trade name, trademark, manufacturer, or otherwise does not necessarily constitute or imply its endorsement, recommendation, or favoring by the United States government or Lawrence Livermore National Security, LLC. The views and opinions of authors expressed herein do not necessarily state or reflect those of the United States government or Lawrence Livermore National Security, LLC, and shall not be used for advertising or product endorsement purposes.

The ion-ion hybrid Alfvén resonator in a fusion environment

W. A. Farmer[1,2] and G. J. Morales[1]

[1]Physics and Astronomy Department,
University of California. Los Angeles
Los Angeles, California 90095

[2]Lawrence Livermore National Laboratory
Livermore, CA 94550, USA

Abstract

An investigation is made of a shear Alfvén wave resonator for burning plasma conditions expected in the ITER device. For small perpendicular scale-lengths the shear mode, which propagates predominantly along the magnetic field direction, experiences a parallel reflection where the wave frequency matches the local ion-ion hybrid frequency. In a tokamak device operating with a deuterium–tritium fuel this effect can form a natural resonator because of the variation in local field strength along a field line. The relevant kinetic dispersion relation is examined to determine the relative importance of Landau and cyclotron damping over the possible resonator parameter space. A WKB model based on the kinetic dispersion relation is used to determine the eigenfrequencies and the quality factors of modes trapped in the resonator. The lowest frequency found has a value slightly larger than the ion-ion hybrid frequency at the outboard side of a given flux surface. The possibility that the resonator modes can be driven unstable by energetic alpha particles is considered. It is found that within a bandwidth of roughly 600 kHz above the ion-ion hybrid frequency on the outboard side of the flux surface, the shear modes can experience significant spatial amplification. An assessment is made of the form of an approximate global eigenmode that possesses the features of a resonator. It is identified that magnetic field shear combined with large ion temperature can cause coupling to an ion-Bernstein wave, which can limit the instability.

PACS: 52.35 Bj, 52.35 Qz, 52.50 Qt, 52.55 Fa, 52.55 Fi

LLNL-JRNL-650395

I. INTRODUCTION

It has long been established that in a plasma containing two ion species, the perpendicular component of the cold-plasma dielectric tensor vanishes at the ion-ion hybrid frequency [1,2],

$$\omega_{ii}^2 = \frac{\omega_{p1}^2\Omega_2^2+\omega_{p2}^2\Omega_1^2}{\omega_{p1}^2+\omega_{p2}^2}, \qquad (1)$$

where ω_{pj} and Ω_j refer, respectively, to the ion plasma frequency and the ion cyclotron frequency of species j. This hybrid frequency acts as a collective resonance for waves propagating across the magnetic field, e.g., the compressional Alfvén wave (or fast wave), and is utilized in schemes for heating the minority ion species in magnetically confined plasmas [3-7]. In contrast, the shear Alfvén wave, which is also referred to as the slow wave, the electromagnetic ion-cyclotron (EMIC) wave, or the ion-ion hybrid wave by different communities, propagates predominantly along the magnetic field. For this reason, the ion-ion hybrid frequency acts as a parallel cutoff for the shear wave and not a resonance. This property is seen from a simplified shear-wave dispersion relation, appropriate for large perpendicular wave numbers $k_\perp$,

$$k_{||}^2 = k_0^2\varepsilon_\perp\left(1-\frac{k_\perp^2}{k_0^2\varepsilon_{||}}\right), \qquad (2)$$

where $k_{||}$ is the parallel wave number for a wave of frequency ω. The vacuum wave number is $k_0 = \omega/c$, with c, the speed of light, and the parallel and perpendicular dielectric tensor components for a cold plasma are $\varepsilon_{||}$ and $\varepsilon_\perp$, respectively. Equation (2) is valid for large perpendicular wave number, satisfying $k_\perp c/\omega_{pj} \gg 1$, so that the perpendicular wavelength is much smaller than the ion skin-depth. When this condition is violated, coupling to the compressional wave occurs, and the dispersion relation must be reformulated with the off-diagonal component of the dielectric tensor, ε_{xy}, included.

Because of the wave cut-off, a propagation gap is created for a cold plasma within the frequency range $\Omega_1 \leq \omega \leq \omega_{ii}$ over which the shear wave is evanescent, where Ω_1 is the cyclotron frequency of the heavier ion species. This separates the propagating frequency range for shear waves into two bands, $\omega < \Omega_1$ and $\omega_{ii} < \omega < \Omega_2$. When a shear wave in the upper frequency band propagates into a region of increasing magnetic field, the wave reflects where the wave frequency matches the local ion-ion hybrid frequency. This reflection has been confirmed by experiments in a linear device [8] and in small tokamaks [9, 10]. For this reason, a magnetic well can form a natural resonator for the shear wave. This idea was first introduced in the context of the earth's magnetosphere, and a resonator spectrum was calculated and compared to satellite observations [11]. Insufficient resolution existed in the

satellite measurements, and the existence of the resonator could not be confirmed. Moiseenko and Tennfors [12], motivated by analogies to low-frequency toroidicity-induced Alfvén eigenmodes (TAE), have considered the role of vanishing $\varepsilon_\perp$ in tokamak geometry. They identified a new class of high-frequency toroidal eigenmodes that they named TLE (TAE-like eigenmodes), but they did not explore the possibility of a resonator. An ion-ion hybrid Alfvén resonator has been verified experimentally in the Large Plasma Device (LAPD) at the University of California, Los Angeles (UCLA) [13]. In that study, shear waves were launched in a linear device with a magnetic well configuration. The quality factors (Q) of the resonances were observed to be between 11 and 18, a value much smaller than expected from cold plasma considerations [14]. In a theoretical study that included both the effects of the off-diagonal component of the dielectric tensor and finite-Larmor-radius (FLR) effects, radial convection of the mode was also unable to explain the low quality factors [15].

Due to the variation in magnetic field strength between the outboard and inboard sides of a toroidal device, a resonator configuration is also naturally present in a tokamak. A preliminary study by the authors [16] surveyed the properties of such a resonator in a burning plasma. The study was limited to a one-dimensional model that neglected Landau and cyclotron damping, and FLR effects. It was concluded that the resonator would be overmoded, and the modes would be localized to the outboard side of the device. A subsequent study applied ray-tracing techniques for parameters relevant to ITER to assess the complicated geometrical effects on the resonator modes [15]. Finite-Larmor-radius effects were included to determine their impact on wave propagation, but damping was excluded from the analysis. It was shown in [15] that the curvature of the field lines preferentially increases the component of the wave vector anti-parallel to the curvature of the field line. With the inclusion of FLR effects, this feature causes the reflection point to change as the absolute magnitude of $k_\perp$ increases. This effect is most pronounced for those modes amenable to ray-tracing, i.e., the resonator eigenmodes that have relatively large quantum numbers.

The existence of an ion-ion hybrid Alfvén resonator in a fusion environment would have relevance to the alpha-channeling concept [17]. Experimental evidence of alpha-channeling has been reported in wave experiments conducted in the Tokamak Fusion Test Reactor (TFTR). In these experiments, energetic deuterium beam ions were used as test particles to examine their interaction with mode-converted ion Bernstein waves [18,19]. Anomalously high loss rates of beam particles were observed. It was proposed that the effect was mediated by an internal eigenmode excited by the ion Bernstein wave (IBW) [20]. Further, the TFTR results showed that fast-ion loss occurred at its greatest level when the mode-conversion layer was close to the axis, but on the outboard side [18]. In principle, such features could be associated with the excitation of the ion-ion hybrid resonator. The basis for the conjecture is a theoretical study by Lashmore-Davies and Russell [21] that showed that the upper-frequency branch of the shear wave can be driven unstable by a superthermal ion distribution. Finally, in recent minority-heating experiments

on Alcator C-Mod, mode conversion into both shear waves and IBWs at the ion-ion hybrid resonance occurred [22], leading to strong toroidal rotation of the plasma. Numerical simulations have been performed to better understand this observed mode conversion process [23].

It is the aim of this study to describe the role of kinetic effects on the ion-ion hybrid resonator and to assess the possibility of an instability driven by a fusion-born alpha population. The results presented here should also guide further studies of both mode-conversion processes and alpha-channeling scenarios.

The manuscript is organized as follows. Section II examines the kinetic dispersion relation for the shear wave in the upper frequency band for parameters relevant to a D-T burning plasma. Section III applies a one-dimensional WKB analysis based on the kinetic dispersion relation for radial profiles from ITER reference scenario-4, type-II [24]. The general eikonal structure of the modes is considered, but in the analysis presented in this section, shear of the magnetic field is neglected. The eigenfrequences of the trapped modes are determined, and kinetic damping is assessed as a function of radius, perpendicular wave number, and mode number. In Sec. IV, an instability due to a superthermal alpha-particle distribution is assessed. The analysis considers the model distribution function for the alpha-particles used by Lashmore-Davies and Russell [21] to calculate the temporal growth, but here the relevant convective amplification is obtained. Section V explores the effect of variations of the perpendicular wave number due to magnetic field shear. Conclusions are presented in Sec. VI.

II. DISPERSION RELATION

Consider a warm plasma with two ion species: deuterium and tritium. The confining magnetic field is chosen to point along the z-direction of a Cartesian coordinate system, (x, y, z), with the wave vector lying in the x-z plane, $\mathbf{k} = k_\perp \hat{\mathbf{x}} + k_{||}\hat{\mathbf{z}}$. The general dispersion relation can be written as

$$\begin{gathered} D_S D_C + D_X - 2k_\perp k_{||}\left[k_0^2 \varepsilon_{yz}\varepsilon_{xy} + \varepsilon_{xz}\left(k^2 - k_0^2\varepsilon_{yy}\right)\right] \\ -2k_0^4 \varepsilon_{xz}\varepsilon_{yz}\varepsilon_{xy} - k_0^2\varepsilon_{yz}^2\left(k_0^2\varepsilon_{xx} - k_{||}^2\right) - k_0^2\varepsilon_{xz}^2\left(k^2 - \varepsilon_{yy}\right) = 0, \end{gathered} \tag{3}$$

where,

$$D_C = k^2 - k_0^2\varepsilon_{yy}, \tag{4}$$

$$D_S = k_0^2\varepsilon_{xx}\varepsilon_{zz} - k_\perp^2\varepsilon_{xx} - k_{||}^2\varepsilon_{zz}, \tag{5}$$

$$D_X = k_0^2\varepsilon_{xy}^2(k_0^2\varepsilon_{zz} - k_\perp^2), \tag{6}$$

with $k^2 = k_\perp^2 + k_{||}^2$. In these expressions, D_C and D_S represent the individual dispersion relations of a pure compressional, and a pure shear root, respectively, with D_X representing coupling between the two modes. The other terms in Eq. (3) are associated with finite ion temperature and are first order or higher in the Larmor radius. To simplify, it is first assumed that the wave frequency is on the order of the ion cyclotron frequencies so that $\omega \sim \Omega_i \ll \omega_{pi} \ll \omega_{pe}, \Omega_e$. Further, the perpendicular wavelength, $\lambda_\perp$, is assumed to be much larger than the electron Larmor radius, ρ_e, so that $k_\perp \rho_e \ll 1$. This allows the electrons to be treated as cold except in the parallel dielectric tensor component, ε_{zz}. Next, it is assumed that the Alfvén speed is much larger than the ion thermal speed. This condition can be cast in the form,

$$\frac{B(\mathrm{kG})^2}{T(\mathrm{keV})n(\mathrm{cm}^{-3})} \gg 10^{-14}, \qquad (7)$$

where B is the confining magnetic field in kiloGauss, T is the plasma temperature in keV, and n is the electron number density. For an ITER-like plasma, $B \approx 50$ kG, $T \approx 10$ keV, and $n \approx 10^{14}$ cm^{-3}, so that the left hand side of Eq. (7) is on the order of 10^{-12} and the condition is satisfied. Further, the toroidal field varies weakly compared to the rapid decreases in temperature and density near the edge, and this relation holds over the whole plasma column. Because of this condition, the off-diagonal components of the dielectric tensor, ε_{xz} and ε_{yz}, can be neglected. With these assumptions, the dispersion relation is simplified to

$$D_S D_C + D_X = 0. \qquad (8)$$

Expressions for the components of the dielectric tensor for a warm plasma can be found in various textbooks, e.g. [25], and are given by

$$\varepsilon_{xx} = 1 + \frac{\omega_{pe}^2}{\Omega_e^2} - \sum_i \frac{\omega_{pi}^2}{\omega^2} \sum_{n=-\infty}^{\infty} \frac{n^2}{\lambda_i} \Lambda_n\big(-x_{0i} Z(x_{ni})\big), \qquad (9)$$

$$\varepsilon_{yy} = \varepsilon_{xx} + 2\sum_i \frac{\omega_{pi}^2}{\omega^2} \sum_{n=-\infty}^{\infty} \lambda_i \Lambda_n{}'\big(-x_{0i} Z(x_{ni})\big)\,, \qquad (10)$$

$$\varepsilon_{xy} = -\frac{\omega_{pe}^2}{\omega\Omega_e} - \sum_i \frac{\omega_{pi}^2}{\omega^2} \sum_{n=-\infty}^{\infty} n\Lambda_n{}'\big(-x_{0i} Z(x_{ni})\big), \qquad (11)$$

$$\varepsilon_{zz} = 1 - \frac{k_{De}^2}{2k_{||}^2} Z'\left(\frac{\omega}{\sqrt{2}k_{||}\bar{v}_e}\right) - \sum_i \left[\frac{\omega_{pi}^2}{\omega^2}\Lambda_0 + \sum_{n\neq 0} \frac{k_{Di}^2}{2k_{||}^2} \frac{\omega - n\Omega_i}{\omega} \Lambda_n Z'\,(x_{ni})\right]. \qquad (12)$$

In the previous expressions, Z is the plasma dispersion function with argument $x_{nj} = (\omega - n\Omega_j)/\sqrt{2}k_{||}\bar{v}_j$, the function, Λ_n, is related to the modified Bessel function, I_n, through the relation, $\Lambda_n(\lambda_j) = I_n(\lambda_j)\exp(-\lambda_j)$ with argument $\lambda_j = k_\perp^2\rho_j^2$, and the Larmor radius defined as $\rho_j = \bar{v}_j/\Omega_j$. The thermal velocities of the relevant species of mass m_j are related to the temperature through $\bar{v}_j = \sqrt{T_j/m_j}$, and the Debye wave number is defined by $k_{Dj} = \omega_{pj}/\bar{v}_j$. Finally, the subscript, j, can represent the electrons, e, or the ions, i, and the cyclotron frequency of the electrons is taken to be positive with the sign explicitly shown.

Equation (8) can be solved numerically for $k_{||}$ as a function of $k_\perp$ and ω in order to examine the field-aligned propagation properties relevant to shear waves. To do so, Newton's method is used to converge upon a solution. An initial guess is required, and this is chosen by finding the solution to Eq. (8) in the inertial limit, i.e., in the limit that $k_{||} \to 0$. In this limit, the components of the dielectric tensor are independent of $k_{||}$, and the plasma dispersion function can be replaced with its asymptotic expression for large argument to yield,

$$\varepsilon_{xx} \Longrightarrow 1 + \frac{\omega_{pe}^2}{\Omega_e^2} + \sum_i \sum_{n>0} \frac{\omega_{pi}^2/\Omega_i^2}{1 - \omega^2/n^2\Omega_i^2} \frac{\Lambda_n}{\frac{1}{2}\lambda_i}, \tag{13}$$

$$\varepsilon_{yy} \Longrightarrow \varepsilon_{xx} - 4\sum_i \sum_{n>0} \frac{\omega_{pi}^2/\Omega_i^2}{1 - \omega^2/n^2\Omega_i^2} \lambda_i \Lambda_n{}', \tag{14}$$

$$\varepsilon_{xy} \Longrightarrow -\frac{\omega_{pe}^2}{\omega\Omega_e} + 2\sum_i \sum_{n>0} \frac{\omega_{pi}^2/\omega\Omega_i}{1 - \omega^2/n^2\Omega_i^2} \Lambda_n{}', \tag{15}$$

$$\varepsilon_{zz} \Longrightarrow 1 - \frac{\omega_{pe}^2}{\omega^2} - \sum_i \left[\frac{\omega_{pi}^2}{\omega^2}\Lambda_0 + 2\sum_{n>0} \frac{\omega_{pi}^2}{\omega^2 - n^2\Omega_i^2}\Lambda_n\right] \approx -\frac{\omega_{pe}^2}{\omega^2}, \tag{16}$$

and the solution to the dispersion relation is given by

$$\frac{k_{||}^2}{k_0^2} = \frac{\varepsilon_{xx} + \varepsilon_{yy}}{2} + \frac{1}{2}\left[\frac{k_\perp^2}{k_0^2}\left(\frac{\omega^2}{\omega_{pe}^2}\varepsilon_{xx} - 1\right) \pm d\right], \tag{17}$$

$$d = \sqrt{\left[\left(\varepsilon_{yy} - \frac{k_\perp^2}{k_0^2}\right) - \varepsilon_{xx}(1 + k_\perp^2\delta_e^2)\right]^2 + 4\varepsilon_{xy}^2(1 + k_\perp^2\delta_e^2)}, \tag{18}$$

where $\delta_e = c/\omega_{pe}$ is the electron skin depth. The appropriate sign must be chosen for the shear root. It is not specified here as the choice depends on the value of the wave frequency relative to the cyclotron frequencies of the individual species.

When Eq. (17) is set to zero, it can be solved for a frequency as a function of the perpendicular wave number. This frequency is a generalization of the ion-ion hybrid frequency at which reflection of the shear wave occurs; it includes FLR effects and the coupling of the shear wave to the compressional wave. At this frequency, for moderate values of $k_\perp$, the wave propagates perpendicular to the magnetic field and is essentially electrostatic in nature, resembling an ion Bernstein wave. However, this mode still exists in the cold plasma limit when FLR effects are negligible and exhibits properties of the shear wave away from this generalized ion-ion hybrid frequency. Thus, Eq. (8) can be solved using the inertial solution as an initial guess near this contour in $(k_\perp, \omega)$ space where the inertial limit is precisely valid and both cyclotron and Landau damping are negligible. Discretizing the parameter space in terms of frequency and perpendicular wave number, Eq. (8) can then be solved by stepping outward from this contour using the closest known solutions to extrapolate a guess for the adjacent point. In evaluating the plasma dispersion function, a technique proposed by Weideman is used [26], supplemented with the asymptotic forms for large argument.

The numerical procedure outlined previously is used to generate Figs. 1-3. The plasma parameters are $n_e = 5.9\times10^{13}$ cm^{-3} and $T_e = 31.1$ keV, with the deuterium and tritium densities, $n_D = n_T = n_e/2$, and temperatures, $T_D = T_T =$ 27.8 keV, and a background magnetic field of $B = 53$ kG. In Fig. 1, the real part of $k_{||}$ is examined. The top panel, Fig. 1(a), shows contours of the real part of the scaled parallel wave number, $k_{||}v_A/\Omega_T$, with the scaled frequency, ω/Ω_T, on the horizontal axis and the scaled perpendicular wave number, $k_\perp\delta_e$, on the vertical axis, where δ_e refers to the electron skin-depth, and v_A is the Alfvén speed. The portion of the parameter space for which the wave is evanescent is represented by the dark (dark-blue in color display) region; the border of this region represents the point at which a parallel cutoff occurs. At small values of $k_\perp\delta_e$, significant coupling to the compressional or fast wave develops, and accordingly the wave propagates over the entire frequency range. At intermediate values of $k_\perp\delta_e$, the cutoff frequency approaches the value given by of the ion-ion hybrid frequency, $\omega_{ii}/\Omega_T = \sqrt{3/2} \approx$ 1.22. At large wave numbers, FLR effects become significant, and the cutoff frequency approaches the cyclotron frequency of tritium. In the middle panel, Fig. 1(b), line-cuts of the contour plot are made at different values of $k_\perp\delta_e$. The horizontal axis is the scaled frequency, and the vertical axis, the real part of the scaled parallel wave number. The cuts are made at the values $k_\perp\delta_e = 0.045$ (solid), 0.145 (dashed), 0.245 (dashed-dotted), and 0.345 (solid with dotted markers). From these line- cuts, the dependence of the cutoff frequency on perpendicular wave number is clear. Further, the parallel wave number rises most rapidly at smaller values of $k_\perp\delta_e$. The bottom panel, Fig. 1(c), displays the argument of the plasma dispersion function, labeled ζ, for the dominant terms that contribute to the damping. The horizontal axis corresponds to the scaled frequency, and the vertical axis, to ζ. For the electrons, represented by the black curves, Landau damping is dominant, thus the parameter, $\zeta = x_{0e}$, is shown. For the ions, damping at the fundamental cyclotron frequency is dominant; accordingly, $\zeta = x_{1i}$ is displayed for

deuterium and tritium, the red and blue curves, respectively. The line styles correspond to the same perpendicular wave number values displayed in the middle panel. Damping is large for the electrons when the parameter, ζ, is close to unity, with the inertial and adiabatic regimes corresponding to $\zeta \gg 1$ and $\zeta \ll 1$, respectively. For the ions, cyclotron damping is greatest when $\zeta = 0$, though cyclotron damping is still significant when $\zeta \sim 1$ and becomes negligible when $\zeta \gg 1$. It is clear that the electrons are adiabatic over most of the frequency range. Strong cyclotron damping due to tritium ions takes place over most of the frequency range, with heavy damping due to deuterium also occurring, peaking at the cyclotron frequency of deuterium, $\omega/\Omega_T = 1.5$. Close to the wave cutoff, all of the damping parameters diverge to infinity due to the vanishing of the parallel wave number, indicating that the waves are undamped.

In Fig. 2, the imaginary part of $k_{||}$ is examined. The top panel, Fig. 2(a), is a contour plot of the imaginary part of the scaled parallel wave number with the scaled frequency on the horizontal axis, and the scaled perpendicular wave number on the vertical axis. In the bottom panel, Fig. 2(b), line-cuts are made of the top panel at various values of the perpendicular wave number. Again, the line-styles correspond to the same values of $k_\perp \delta_e$ as in Fig. 1(b). At small values of $k_\perp \delta_e$, where coupling to the compressional wave is strong, the damping is weak. As the value of $k_\perp \delta_e$ increases and the wave begins to exhibit properties of the shear wave, the damping becomes significant. As $k_\perp \delta_e$ increases further, the absolute magnitude of the damping decreases. To assess the effect of damping on the resonator, the parameter, $\eta = 2\pi\, \mathrm{Im}(k_{||})/\mathrm{Re}(k_{||})$, is evaluated; it measures the amount of damping experienced in one parallel wavelength. This quantity is shown in Fig. 3. The top panel, Fig. 3(a), is a contour plot of the relative damping, with the scaled frequency on the horizontal axis and the scaled perpendicular wave number on the vertical axis. The white curve corresponds to the value $\eta = 1$. Signals in the region to the right of this curve damp by more than one e-folding in a wavelength. The region to the left of the white contour is weakly damped, and candidate resonator modes may occur in this portion of the parameter space. The bottom panel, Fig. 3(b), shows line-cuts of the top panel at different values of $k_\perp \delta_e$, with the line-styles corresponding to the same values as in Fig. 1(b).

III. WKB ANALYSIS

In analyzing the resonator modes, a cylindrical approximation of the tokamak geometry is made. In this approximation, the magnetic flux surfaces are concentric circles of radius, r, centered on the magnetic axis. The poloidal angle is θ, and in these coordinates, the toroidal field has the dependence,

$$B_t = \frac{B_0}{1 + \frac{r}{R}\cos\theta}, \tag{19}$$

where R is the major radius and B_0 is a characteristic value for the toroidal field. The safety factor is defined by

$$q(r) = \frac{rB_0}{RB_p}. \tag{20}$$

The total magnetic field strength is given by

$$B = B_t\sqrt{1 + \frac{B_p^2}{B_t^2}} = B_t\sqrt{1 + \left(\frac{r}{q(r)R}\right)^2} \approx B_t. \tag{21}$$

In this expression, the small aspect ratio approximation is made, and it is sufficient to approximate the total magnetic field strength as due to the toroidal field alone. Within this approximation, the distance traversed by a field line is related to the poloidal coordinates through the relation,

$$s = \theta\sqrt{R^2q(r)^2 + r^2} \approx Rq(r)\theta. \tag{22}$$

Profiles for the electron density, safety factor, and electron and ion temperatures are found from simulation results reported in Fig. 41(c) and (d) of Gormezano et al. [24]. The profiles were originally reported as functions of the scaled variable, x, which relates to the flux coordinate, Φ, through the relation $x = (\Phi/\pi a^2 B_t)^{1/2}$. In the cylindrical approximation, this reduces to $x = r/a$. The resulting profiles are reproduced here in the cylindrical approximation as shown in Figs. 4 with the minor radius chosen to be $a = 200$ cm. The top panel, Fig. 4(a), shows the electron density (solid curve) and the safety factor (dashed curve). The vertical axis on the left corresponds to the electron density, and on the right, to the safety factor. The horizontal axis, common to both pannels, is the radius from the magnetic axis. The bottom panel, Fig. 4(b), displays the electron (solid curve) and ion (dashed curve) temperatures, with the vertical axis corresponding to temperature and the horizontal axis to the radius from the magnetic axis. These profiles are used to extract reasonable estimates of the type of behavior expected in a burning plasma.

With these profiles specified, a WKB method is implemented. In this section, the effects of magnetic shear are neglected, and the perpendicular wave number, $k_\perp$, is assumed constant. The effects of shear are considered later in Sec. V. Because the shear Alfvén mode predominantly propagates parallel to the magnetic field, the modes are assumed to be localized about a radius, r. For this reason, a one-dimensional model is adopted in which the spatial dependence appearing in the wave equation is due to the variations in magnetic field strength along a field line, from the outboard to the inboard side. In this approximation, the generic wave equation takes the form,

$$\frac{d^2\Psi}{ds^2} + \mathrm{Re}\left[k_{||}^2(s,\omega_n,k_\perp)\right]\Psi = 0, \tag{23}$$

where Ψ represents the characteristic amplitude of the shear wave. The compressional wave is excluded in this formulation in an effort to determine the intrinsic properties of the shear wave. Mode conversion effects should also be described in a future comprehensive study of the trapped modes, but are not considered here. The damping is assumed to be weak in this model and is treated as a higher order correction in order to determine the quality factor, Q, of the resulting modes. If, a posteriori, this assumption is violated, i.e., the resulting quality factor is small, such modes cannot be considered candidate resonator modes. Thus, to zeroth-order, the WKB quantization condition is given by

$$\int_{-s_0(\omega_n)}^{s_0(\omega_n)} \mathrm{Re}\left[k_{||}^2(s,\omega_n,k_\perp)\right] ds = \left(n + \frac{1}{2}\right)\pi, \tag{24}$$

where $s_0(\omega)$ is the distance along a field line, measured from the outboard side, at which the wave is expected to reflect; it corresponds to the position determined from Eq. (17) where $k_{||} = 0$. The value of $k_{||}$ is determined by solving Eq. (8) along the field line trajectory. The constant, n, takes on integer values beginning at zero, and corresponds to the quantum number of the trapped mode with eigenfrequency, ω_n. The WKB approximation is known to work best for modes with large quantum numbers. For modes of small quantum number, an alternative formulation can be used in which the parallel wave number is approximated locally as a parabolic potential,

$$\mathrm{Re}\left[k_{||}^2(s)\right] = V(s) \approx V(0) + \frac{1}{2}V''(0)s^2. \tag{25}$$

The well known quantization condition for such an effective potential is

$$\sqrt{-\frac{2}{V''(0)}}V(0) = 2n + 1. \tag{26}$$

For the present application it is found that the difference between the fundamental frequencies found by the WKB method and the parabolic fit differ typically by a factor on the order of 0.1%. For this reason, in what follows the WKB method is applied. However, an advantage in the parabolic approximation is that analytic eigenfunctions result for the fundamental modes. These functions could be used in a future study to construct approximate full-wave solutions for these modes.

To determine an approximate form for the quality factor, the axial WKB-eigenfunction inside the well is first examined. This takes the form

$$\Psi \propto \frac{2}{\sqrt{k_{||}(s)}} \sin\left[\int_{s}^{s_0} k_{||}(s')ds' + \frac{\pi}{4}\right]. \tag{27}$$

Utilizing the quantization condition given in Eq. (24), this can be rewritten as

$$\Psi \propto \frac{1}{\sqrt{k_{||}(s)}} e^{-i\pi/4} \left[e^{i\int_{-s_0}^{s} k_{||}(s')ds'} \pm e^{-i\int_{s_0}^{s} k_{||}(s')ds'}\right], \tag{28}$$

where the sign choice depends on the evenness or oddness of the specific mode, and is unimportant for the present purposes. The form of the eigenfunction can be interpreted as an incident wave from the left superposed with a reflected wave traveling from the right. Variations in the amplitude are associated with the changes in wave velocity. Considering $k_{||}$ to be complex at this point, the wave amplitude decrease largely due to the phase factors present in the exponential functions. Upon each round trip, the wave amplitude is reduced by a factor of

$$e^{-2\int_{-s_0}^{s_0} \mathrm{Im}\,[k_{||}(s')]ds'}. \tag{29}$$

Thus, if a source is continually pumping the system with an input power of $P = \omega|\Psi_0|^2$, the stored energy in the resulting wave is

$$E = \frac{|\Psi_0|^2}{\left[1 - e^{-2\int_{-s_0}^{s_0} \mathrm{Im}\,[k_{||}(s')]ds'}\right]^2}. \tag{30}$$

The quality factor is approximated as

$$Q \sim \frac{1}{\left[1 - e^{-2\int_{-s_0}^{s_0} \mathrm{Im}\,[k_{||}(s')]ds'}\right]^2}. \tag{31}$$

Although only kinetic sources of dissipation are considered here, the actual quality factor in an experiment likely also exhibits a reduction due to radial convection of the wave and mode conversion at the reflection point.

Figure 5 shows the calculated eigenfrequencies as a function of radius. For these results, the magnetic field strength is given by Eq. (19) with the characteristic strength of the toroidal field taken to be $B_0 = 53$ kG, and equal concentrations of deuterium and tritium are assumed with quasineutrality satisfied. The perpendicular wavelength is taken to be $\lambda_\perp = 10$ cm, which gives a scaled perpendicular wave number of $k_\perp \delta_e = 0.0431$ at the magnetic axis. This scaled value increases as the density slowly decreases towards the plasma edge. In the top

panel, Fig. 5(a), the horizontal axis corresponds to radial distance from the magnetic axis, and the vertical axis, to frequency in MHz. The lower solid black curve, labeled by ω_0, gives the fundamental frequency of the resonator at a given value of the outboard radius of a magnetic surface. Due to the overmoding that occurs, the cutoff frequency at the outboard position is in close proximity to this value. Immediately above this curve, the red line, labeled by $\omega_{Q=20}$, represents the frequency of modes having a quality factor $Q = 20$. Above this red dashed line there is cross-hatching (blue in color) that indicates the region of heavily damped modes. In practice the frequency of candidate resonator modes lies in the narrow strip between the bottom solid curve and the dashed line. The slanted green line labeled by ω_{Max} corresponds to the largest frequency for which a reflection could occur on the inboard side, i.e., the cutoff frequency on the inboard side. At larger radii, this frequency is greater than the deuterium cyclotron frequency on the inboard side, and loses meaning. For this reason, the line is terminated when it intersects this cyclotron frequency. For reference, the cyclotron frequency of deuterium on the inboard side is represented by the top orange curve. From this display, it is clear that within this description, long-lived resonator modes exist in a narrow frequency bandwidth, of roughly 200 – 300 kHz, near the cutoff frequency on the outboard side. In the bottom panel, Fig. 5(b), the number of trapped modes as a function of radius is shown. The horizontal axis corresponds to the distance from the magnetic axis, and the vertical axis, to the number of modes. The solid curve corresponds to the maximum number of modes, $n_{Q>20}$, having quality factors, Q, greater than 20. This number stays around 15-30 over the domain shown; modes with larger quantum numbers are heavily damped and are not expected to be excited.

The quality factors of the fundamental modes calculated for the parameters associated with Fig. 5 are found to be in the range of $Q > 10^6$ across the entire plasma column. Such large values of Q are, of course, not realistic, and simply indicate that wave-particle damping due to electron Landau resonance and ion cyclotron resonance is negligible for these modes. To determine the realistic quality factor for these modes, a consideration of radial convection of wave energy and mode conversion processes is necessary.

Figure 6 displays the dependence of the quality factor on mode number. For the solid curve, the parameters are the same as in Fig. 5, with the calculation performed at $r = 50$ cm, which corresponds to an electron temperature of $T_e = 31.1$ keV and a scaled perpendicular wave number of $k_\perp \delta_e = 0.0433$. For the dashed curve, the same parameters are used, with the exception that the ion and electron temperatures are both decreased proportionally so that the peak electron temperature on axis is 10 keV. This corresponds to an electron temperature of $T_e = 8.39$ keV at $r = 50$ cm, where the calculation is performed. Finally, the dash-dotted curve is calculated with the same parameters as the solid curve, except that the perpendicular wavelength is decreased to $\lambda_\perp = 3$ cm, resulting in a scaled perpendicular wave number of $k_\perp \delta_e = 0.1443$. As mentioned previously, wave-particle interactions are negligible for low mode numbers; these undamped modes

will be limited in actual experiments by other processes. For definiteness, an undamped mode is considered here to be a mode for which $Q > 100$. For this reason, the vertical axis in Fig. 6 is scaled to have Q=100 as its maximum value. The undamped modes correspond to $n \leq 8$ for the solid line, $n \leq 13$ for the dashed line, and $n \leq 1$ for the dash-dotted line. The curves rise rapidly towards unrealistic large values near the fundamental mode, $n = 0$. From Fig. 6 it is seen that decreasing the temperature decreases the damping, as expected, and that decreasing the perpendicular wavelength increases the damping. This is primarily due to the decrease in the rise of the real part of $k_{||}$, as shown in Fig. 2(b), which causes the eigenfrequencies to shift away from the cutoff frequency. This upshift in frequency leads to an increase in the relative damping, shown in Fig. 3(a). Figure 7 shows the number of modes that are not heavily damped at $r = 10$ cm. The vertical axis corresponds to the number of modes with $Q > 20$, and the horizontal axis, the scaled perpendicular wave number. The parameters used are the same as those used for Fig. 6 with the exception that the perpendicular wave number now varies.

Figure 8 illustrates the poloidal extent of the modes. The horizontal axis corresponds to the radius of the given flux surface at which the calculation is performed, and the vertical axis corresponds to the poloidal angular (in degrees) extent of the corresponding mode. The solid curve corresponds to the fundamental mode, and the dashed line corresponds to a mode for which $Q = 20$. The angle spanned by the fundamental mode decreases monotonically, rising sharply towards the magnetic axis. The fundamental mode is largely localized poloidally over all of the flux surfaces, except in a very narrow region near the center. The dashed line exhibits similar trends, except that it rises sharply near the edge. This is due to the rapid decrease in the density and temperature of the plasma. While this mode spans a much larger poloidal angle, it is still largely localized over most of the flux surfaces.

IV. INSTABILITY DUE TO SUPERTHERMAL ALPHA-PARTICLES

In this section a methodology similar to that introduced by Lashmore-Davies and Russell [21] is used to assess the possibility that fusion-born alpha particles can drive the resonator modes unstable. The difference in the present study is that spatial amplification is considered for a fixed real frequency, and medium nonuniformities are retained within a WKB description. Instability corresponds to $\mathrm{Im}[k_{||}] < 0$, with $\mathrm{Re}[k_{||}] > 0$, i.e., the wave grows in the direction of propagation.

The alpha particles are assumed to be a perturbation on the wave propagation properties, with the alpha particle density taken to be the expansion parameter. Terms that are first order in this density are retained, and higher order terms are neglected. To perform this expansion, the dielectric tensor components are separated into a zeroth order contribution, $\varepsilon_{ij}^{(0)}$, and a first order contribution,

$\varepsilon_{ij}^{(1)}$. The components, xz and yz, do not have a zeroth order contribution, because they do not enter into the zeroth-order dispersion relation, considered in Sec. II. For this reason, the last three terms on the bottom line of Eq. (3) are neglected. Keeping terms to first order,

$$D_C = D_C^{(0)} - k_0^2 \varepsilon_{yy}^{(1)}, \tag{32}$$

$$D_S = D_S^{(0)} + \left[\varepsilon_{xx}^{(1)}\left(k_0^2 \varepsilon_{zz}^{(0)} - k_\perp^2\right) + \varepsilon_{zz}^{(1)}\left(k_0^2 \varepsilon_{xx}^{(0)} - k_{||}^2 \varepsilon_{zz}^{(0)}\right)\right], \tag{33}$$

$$D_X = D_X^{(0)} + 2k_0^2 \varepsilon_{xy}^{(1)} \varepsilon_{xy}^{(0)}\left(k_0^2 \varepsilon_{zz}^{(0)} - k_\perp^2\right) - k_0^4 \varepsilon_{zz}^{(1)}\left(\varepsilon_{xy}^{(0)}\right)^2, \tag{34}$$

where the zeroth order terms for $D_C^{(0)}$, $D_S^{(0)}$, and $D_X^{(0)}$ are defined in Eqs. (4)-(6), with the dielectric coefficients evaluated with their zeroth order forms. With these expressions, the dispersion relation, to first order, is

$$D = D^{(0)} + D^{(1)}, \tag{35}$$

$$D^{(0)} = D_C^{(0)} D_S^{(0)} + D_X^{(0)}, \tag{36}$$

$$\begin{aligned} D^{(1)} = {} & -k_0^2 \varepsilon_{yy}^{(1)} D_S^{(0)} + \left(k_0^2 \varepsilon_{zz}^{(0)} - k_\perp^2\right)\left[\varepsilon_{xx}^{(1)} D_C^{(0)} + 2k_0^2 \varepsilon_{xy}^{(1)} \varepsilon_{xy}^{(0)}\right] \\ & + \varepsilon_{zz}^{(1)}\left(k_0^2 \varepsilon_{xx}^{(0)} - k_{||}^2\right) D_C^{(0)} - k_0^4 \varepsilon_{zz}^{(1)}\left(\varepsilon_{xy}^{(0)}\right)^2 - 2k_\perp k_{||}\left[k_0^2 \varepsilon_{yz}^{(1)} \varepsilon_{xy}^{(0)} + \varepsilon_{xz}^{(1)}\left(k^2 - k_0^2 \varepsilon_{yy}^{(0)}\right)\right]. \end{aligned} \tag{37}$$

Next, $k_{||}$ is similarly be expanded as $k_{||} = k_{||}^{(0)} + k_{||}^{(1)}$. Upon Taylor expanding D about $k_{||}^{(0)}$, and solving for the first order correction,

$$k_{||}^{(1)} = -\frac{D^{(1)}\left(k_{||}^{(0)}\right)}{\left.\frac{\partial D^{(0)}}{\partial k_{||}}\right|_{k_{||}^{(0)}}}. \tag{38}$$

This allows the first order correction to be determined for the zeroth-order mode described in Sec. III. Instability arises in those portions of the device where $\mathrm{Im}\left[k_{||}^{(0)} + k_{||}^{(1)}\right] < 0$, indicating that drive from the alpha particles must overcome the kinetic damping caused by the background plasma.

To model the fusion-born alpha particles, a ring-distribution is used. This could have relevance for the core plasma of a tokamak in the immediate post-birth

phase before collisional relaxation can occur, and is therefore, of interest to the alpha-channeling question. It takes the form,

$$f_\alpha(v_\perp, v_{||}) = n_\alpha \left(\frac{1}{2\pi v_{\perp\alpha}} \delta(v_\perp - v_{\perp\alpha}) \right) \left(\frac{1}{\sqrt{2\pi}\bar{v}_{||\alpha}} e^{-\frac{v_{||}^2}{2\bar{v}_{||\alpha}^2}} \right), \tag{39}$$

where n_α is the density of the alpha particles, and $v_{\perp\alpha}$ and $\bar{v}_{||\alpha}$ are characteristic velocities for the distribution. These velocities can be related to an effective temperature through $T_{\perp\alpha} = m_\alpha v_{\perp\alpha}^2/2$ and $T_{||\alpha} = m_\alpha \bar{v}_{||\alpha}^2/2$, where $T_{\perp\alpha} + T_{||\alpha} =$ 3.5 MeV, the energy of an alpha particle following a DT fusion event. This distribution function is used to obtain the contribution to the dielectric tensor from the alpha particles. The form of this contribution can be cast in terms of integrals over the perpendicular and parallel velocity directions, which are readily evaluated [25]. The result is

$$\varepsilon_{xx}^{(1)} = \frac{\omega_{p\alpha}^2}{\omega^2} \sum_n \left\{ \left[-1 + \frac{n\Omega_\alpha}{\sqrt{2}k_{||}\bar{v}_{||\alpha}} Z(x_{n\alpha}) \right] P_n + [1 + x_{n\alpha} Z(x_{n\alpha})] \frac{v_{\perp\alpha}^2}{\bar{v}_{||\alpha}^2} \frac{n^2 J_n^2}{k_\perp^2 \rho_\alpha^2} \right\}, \tag{40}$$

$$\varepsilon_{xy}^{(1)} = i \frac{\omega_{p\alpha}^2}{\omega^2} \sum_n \left\{ \left[-1 + \frac{n\Omega_\alpha}{\sqrt{2}k_{||}\bar{v}_{||\alpha}} Z(x_{n\alpha}) \right] Q_n + [1 + x_{n\alpha} Z(x_{n\alpha})] \frac{v_{\perp\alpha}^2}{\bar{v}_{||\alpha}^2} \frac{n J_n J_n'}{k_\perp \rho_\alpha} \right\}, \tag{41}$$

$$\varepsilon_{yy}^{(1)} = \frac{\omega_{p\alpha}^2}{\omega^2} \sum_n \left\{ \left[-1 + \frac{n\Omega_\alpha}{\sqrt{2}k_{||}\bar{v}_{||\alpha}} Z(x_{n\alpha}) \right] R_n + [1 + x_{n\alpha} Z(x_{n\alpha})] \frac{v_{\perp\alpha}^2}{\bar{v}_{||\alpha}^2} J_n'^2 \right\}, \tag{42}$$

$$\varepsilon_{xz}^{(1)} = -\frac{1}{2} \frac{\omega_{p\alpha}^2}{\omega^2} \frac{k_\perp}{k_{||}} \sum_n Z'(x_{n\alpha}) \left[n^2 P_n + \frac{\omega - n\Omega_\alpha}{\Omega_\alpha} \frac{v_{\perp\alpha}^2}{\bar{v}_{||\alpha}^2} \frac{n J_n^2}{k_\perp^2 \rho_\alpha^2} \right], \tag{43}$$

$$\varepsilon_{yz}^{(1)} = -\frac{i}{2} \frac{\omega_{p\alpha}^2}{\omega^2} \frac{k_\perp}{k_{||}} \sum_n Z'(x_{n\alpha}) \left[n S_n - \frac{\omega - n\Omega_\alpha}{\Omega_\alpha} \frac{v_{\perp\alpha}^2}{\bar{v}_{||\alpha}^2} \frac{J_n J_n'}{k_\perp \rho_\alpha} \right], \tag{44}$$

$$\varepsilon_{zz}^{(1)} = -\frac{\omega_{p\alpha}^2}{\omega^2} + \frac{\omega_{p\alpha}^2}{\omega^2} \sum_n \left\{ [1 - x_{n\alpha}^2 Z'(x_{n\alpha})] U_n - Z'(x_{n\alpha}) \frac{\bar{v}_{||\alpha}^2}{v_{\perp\alpha}^2} x_{0\alpha} k_\perp \rho_\alpha J_n J_n' \right\}, \tag{45}$$

where the notation used in Eqs. (9)-(12) has been adopted, with the definitions of $x_{n\alpha}$ and ρ_α generalized to $x_{n\alpha} = (\omega - n\Omega_j)/\sqrt{2}k_{||}\bar{v}_{||\alpha}$ and $\rho_\alpha = v_{\perp\alpha}/\Omega_\alpha$, and where J_n is a Bessel function with argument $k_\perp \rho_\alpha$. The remaining undefined parameters are,

$$P_n = \frac{2}{k_\perp \rho_\alpha} J_n J_n', \tag{46}$$

$$Q_n = nJ_n'^2 + \left(\frac{n^2}{k_\perp^2\rho^2} - 1\right)J_n^2, \tag{47}$$

$$R_n = \frac{2n^2}{k_\perp\rho}\left(1 - \frac{k_\perp^2\rho^2}{n^2}\right)J_nJ_n', \tag{48}$$

$$S_n = J_n'^2 + J_n^2\left(\frac{n^2}{k_\perp^2\rho^2} - 1\right), \tag{49}$$

$$U_n = \frac{1}{2}J_n^2 - \frac{\bar{v}_{||\alpha}^2}{v_{\perp\alpha}^2}k_\perp\rho_\alpha J_nJ_n'. \tag{50}$$

After examining the relative importance of the various terms presented in Eqs. (40)-(45), it is determined that the most important term for instability is $\varepsilon_{xx}^{(1)}$. This is not surprising, because at these large values of $k_\perp$, coupling to the compressional wave is largely negligible. Upon examination of Eq. (39), it is apparent that the possibility of amplification is determined primarily by the sign of $P_{n=1}$, with the fundamental cyclotron frequency being the dominant contributor in this frequency range.

In order to making comparisons to the results of Lashmore-Davies and Russell [21], we choose plasma parameters corresponding to $r = 50$ cm in Fig. 5: $B = 49.1$ kG, $n_e = 5.9\times10^{13}$ cm^{-3}, $T_e = 31.1$ keV, $T_D = T_T = 27.8$ keV, $T_{\perp\alpha} = 2$ MeV, $T_{||\alpha} = 1.5$ MeV, and $n_\alpha = 0.01n_e$. The ion densities preserve quasineutrality through the relation, $n_D = n_T = n_e/2 - n_\alpha$. Figure 9 explores the possibility of amplification for two values of $k_\perp$. On the horizontal axis is the scaled frequency, ω/Ω_T, and on the vertical axis is the imaginary part, $\mathrm{Im}[k_{||}]$. The solid and dashed curves correspond to $k_\perp\rho_\alpha = 2.5$ and 4.5, $k_\perp\delta_e = 0.044$ and 0.080, $\lambda_\perp = 9$ and 5 cm, respectively. The local extrema of the curves immediately adjacent to the cutoff in Fig. 9 occurs when $x_{1\alpha}\sim -1$, so that the alpha particle contribution possesses a significant imaginary part but the background deuterium is still far from cyclotron resonance, a conclusion which agrees with the work of Lashmore-Davies and Russell [21]. From the sign of P_1, the intervals of $k_\perp\rho_\alpha$, which correspond to instability, can be determined. These fall between the peak and successive zero of the Bessel function, J_1. The first two intervals are $k_\perp\rho_\alpha \in$ (1.84,3.83) and $k_\perp\rho_\alpha \in$ (5.33,7.02). It is seen from Fig. 9 that the value of $k_\perp\rho_\alpha$, which is within the first interval corresponds to strong instability, i.e., the curve falls below the y-axis for a portion of the frequency domain. The value of $k_\perp\rho_\alpha$ that falls outside these two intervals is damped. The second interval of $k_\perp\rho_\alpha$ for which $J_1 < 0$ exhibits much weaker instability with $\mathrm{Im}[k_{||}]$ reaching a minimum negative value roughly an order of magnitude less than the solid line in Fig. 9. This is because of the larger cyclotron damping that occurs in the background plasma at smaller perpendicular wavelengths. A critical density for these two intervals of $k_\perp\rho_\alpha$ can now be

determined using the condition for marginal stability, $\mathrm{Im}\left[k_{||}^{(0)} + k_{||}^{(1)}\right] = 0$, where $k_{||}^{(1)}$ is assumed to be at the critical density, $n_{\alpha c}$. So long as the perturbative model is valid, $k_{||}^{(1)}$ is linear in n_α. Thus, the marginal stability condition can be rewritten as

$$\mathrm{Im}\left[k_{||}^{(0)} + k_{||}^{(1)}(n_\alpha)\frac{n_{\alpha c}}{n_\alpha}\right] = 0. \tag{51}$$

This condition is scanned in frequency to determine the smallest critical density, while choosing the value of $k_\perp$ for which P_1 is most negative within the interval of interest. This procedure results in the critical densities $n_\alpha/n_e = 7.3\times10^{-5}$ for the first interval, and $n_\alpha/n_e = 3.6\times10^{-3}$ for the second, but it should be emphasized that these densities are obtained at $r = 50$ cm, and these values will vary with radius. Simulations of expected conditions for burning plasmas in ITER predict that the alpha density will be 0.85% of the electron density on the magnetic axis [27]. This justifies the use of the alpha density as an expansion parameter. In the analysis that follows, values of $k_\perp$ are chosen that fall in the interval of largest instability.

Next, the results of the stability analysis are related to the ion-ion hybrid resonator in ITER. An amplification factor is defined as,

$$A = -\int_{-s_0}^{s_0} \mathrm{Im}[k_{||}]ds, \tag{52}$$

indicating the exponential factor that a wave grows (or damps) during a single pass through a resonator of total length $2s_0$. If $A > 0$, this indicates that the drive of the alpha particles is greater than the damping on the background plasma. In Fig. 10, the imaginary part of $k_{||}$ is displayed for five resonator modes at a radial position of $r = 50$ cm, where the profiles specified in Figs. 4 are used. This corresponds to the parameters, $n_e = 5.95\times10^{13}$ cm^{-3}, $T_e = 31.1$ keV, and $T_i = 27.8$ keV. The magnetic field on the outboard side of the flux surface is $B = 49.1$ kG. For the alpha particles, the same parameters are used as in Fig. 9. The perpendicular wavelength is chosen to maximize instability drive, minimizing P_1 .The horizontal axis corresponds to the distance spanned by the mode along a field line, and the vertical axis to the imaginary part of $k_{||}$ with both the zeroth order term and first order correction included. The dashed, solid, and dashed-dotted curves correspond to three different trapped modes, $n = 7, 17,$ and 27 with amplification factors, $A = 2.6, 3.1,$ and 2.6, respectively. At this position, the $n = 2 - 34$ modes have positive amplification factors and exhibit a narrow frequency range of $f = 30.38 - 30.96$ MHz , with $n = 17$ the most unstable. The spatial undulations of the growth coefficient seeing in Fig. 10 arise due to the lengthening of the resonator, maximizing cyclotron resonance with the alpha particles, and minimizing cyclotron damping on the background plasma. At small n numbers, cyclotron resonance with the alpha particles is not possible because $k_{||}$ is too small over the resonator region. Thus, the

first unstable mode appears at $n = 2$. As the mode number increases, the mode comes into cyclotron resonance with the alpha particles and the resonator-length increases, leading to maximum amplification at $n = 17$. As the mode number increases beyond this value, cyclotron damping on the background ions becomes dominant and inhibits amplification of the resonator modes.

In order to illustrate the frequency bandwidth of amplified resonator modes at different radii, Fig. 11 displays the amplification factor, A, versus frequency at four different radii. The four solid curves correspond to $r = 25$, 50, 100, and 150 cm, and are labeled accordingly. At each radius, the bandwidth of the amplified modes is roughly 600 kHz, with the frequency of greatest amplification shifting to lower frequencies at larger radii, as expected from the eigenfrequency outline in Fig. 5(a). Amplification of the modes is seen to increase towards the core and the edge. The increase towards the core is a geometrical effect, which lengthens the resonator. The increase towards the edge is due to decreased damping due to the lower temperatures; however, the density of the fusion-born alpha population should significantly decrease at these larger radii, likely limiting the amplification experienced by the modes. Finally, it should be mentioned that while the amplified frequencies are shown only at four different radii, the radius of the flux surface is a continuous variable. For this reason, the eigenfrequencies of the resonator become a continuous function of radius, and amplified frequencies for the entire plasma column can vary over several MHz.

V. EFFECTS OF SHEAR

To explore the effects of magnetic field shear, an attempt is made to determine the structure of the eigenmodes in the global geometry of the tokamak. To do so, an eikonal form for the wave field is assumed, similar to that which is commonly used in ballooning-mode analysis. This takes the form

$$\mathbf{E} = \mathbf{E}_S e^{i\psi}, \tag{54}$$

where ψ is the rapidly varying eikonal and $\mathbf{E}_S$ is the eigenvector which corresponds to the shear Alfvén wave root. The amplitude of the eigenvector, $\mathbf{E}_S$, is assumed to vary much slower than ψ. In this approximation, the wave number is related to the eikonal through $\mathbf{k} = \nabla\psi$. The poloidal coordinates are defined in the cylindrical approximation as in Sec. III to be (r, θ). The toroidal angle is taken to be ϕ. This allows for the eikonal to be written as

$$\psi = \int k_{||}(r, s)ds + m[\phi - q(r)(\theta - \theta_0)] + k_r r, \tag{55}$$

where m corresponds to a Fourier decomposition of the modes in the toroidal coordinate. This is done because azimuthal symmetry of the equilibrium profile is assumed. Further, k_r is assumed constant, corresponding to the radial wave number, and s is a coordinate, which measures the relative distance along a respective field

line. Coordinate surfaces are defined in a similar manner to nonlinear simulations of tokamak turbulence using flux tubes [28]. The orthogonal coordinate surfaces are described by the variables, r, corresponding to a unique flux surface, $\alpha = \varphi - q(r)(\theta - \theta_0)$, which, for constant r, uniquely specifies a field line, and s, defined to be orthogonal to the other coordinate surfaces; $s = 0$ is chosen to correspond to the outboard side of the tokamak. An approximate form for s is given in Eq. (22). From this form, it is apparent that if a Fourier decomposition of Eq. (55) is performed in the poloidal angle through the basis functions, $\exp(il\theta)$, the result would contain many values of l because the modes are poloidally localized to the outboard side. The quantity $k_{||}$ is independent of α, because, for fixed r and s, the dispersion relation is invariant with respect to the field line chosen. With Eq. (55), the wave vector is determined to be,

$$\mathbf{k} = k_{||}\hat{\mathbf{b}} + k_t\hat{\mathbf{t}} + k_n\hat{\mathbf{r}}, \tag{56}$$

$$k_t = m\frac{B}{RB_p} \approx m\frac{q(r)}{r}, \tag{57}$$

$$k_n = \frac{\partial}{\partial r}\left[\int k_{||}ds\right] - mq'(r)(\theta - \theta_0) + k_r, \tag{58}$$

where the unit vectors are $\hat{\mathbf{r}}$, normal to the flux surfaces, $\hat{\mathbf{t}} = \widehat{\boldsymbol{\phi}}\, B_p/B - \widehat{\boldsymbol{\theta}}\, B_t/B$, lying in the geodesic direction, and $\hat{\mathbf{b}} = \widehat{\boldsymbol{\phi}}\, B_t/B + \widehat{\boldsymbol{\theta}}\, B_p/B$, lying parallel to the magnetic field. The perpendicular wave number, $k_\perp = \sqrt{k_t^2 + k_n^2}$, is now seen to vary with position. It should be mentioned that since $\hat{\mathbf{t}}$ lies predominantly in the $\widehat{\boldsymbol{\theta}}$ direction, k_t can be approximately interpreted as the poloidal wave number. Further, choosing m to be an integer preserves periodicity in the toroidal direction. Subtle issues involving periodicity requirements for the poloidal angle are unimportant to the trapped modes examined here, because they exhibit strong localization in the poloidal direction.

To apply this method, an iterative process is used in which the variable s is first discretized. The outboard location, $s = 0$, is chosen as a starting point at which the value of k_n is specified. The new value of k_n is computed at the adjacent grid point using the value of $k_{||}$ at the initial point. This new value of k_n is then used to compute $k_{||}$ at the new point, thus the method resembles a finite difference scheme. Using Eq. (22) to express Eq. (58) as a function of s, yields

$$k_n = \frac{\partial}{\partial r}\left[\int k_{||}ds\right] - \frac{mq'(r)}{Rq(r)}(s - s_0) + k_r. \tag{59}$$

With this form, the difference scheme becomes

$$k_n^{(j+1)} = k_n^{(j)} + \left[\frac{\partial k_{||}^{(j)}}{\partial r} - \frac{mq'(r)}{Rq(r)}\right] ds. \tag{59}$$

For definiteness, θ_0 and k_r are defined to vanish at the outboard location. This is done to minimize radial propagation of the mode so that perpendicular propagation initially occurs solely in the geodesic direction. As the wave evolves, it develops a nonzero component of k_r, which causes the energy to travel radially because of the non-ideal feature of the shear Alfvén waves in this regime.

First, to provide insight into the role of magnetic shear, the methodology is applied to an idealized cold plasma. Figure 12 illustrates the calculated parallel and perpendicular wave numbers as a function of the variable s. The magnetic well is examined at the radius $r = 50$ cm, with electron density, $n_e = 5.9\times10^{13}$ cm^{-3}, and safety factor, $q = 1.45$. The frequency of the wave is chosen to be $\omega = 1.01\omega_{ii}$, where ω_{ii} is given by Eq. (1) with the cyclotron frequencies evaluated at $s = 0$. The solid, dashed, and dash-dotted curves in the top and bottom panels correspond to the m-numbers, $m = 4, 8$, and 12. The choice of m results in a minimum value for the absolute magnitude of $k_\perp$ because k_t is unaffected by the magnetic shear, as seen in Eq. (57). Increasing m causes the wave to begin with a larger initial $k_\perp$, thus, minimizing coupling to the compressional wave. In the top panel, Fig. 12(a), the vertical axis corresponds to $k_{||}^2$, and in the bottom panel, Fig. 12(b), the vertical axis corresponds to the scaled perpendicular wave number, $k_\perp\delta_e$. It is seen from the top panel that the there is little variation in the cutoff point for the three cases. This arises because, in the cold plasma case, variations in the cutoff position are caused by coupling to the compressional mode. At the cutoff location, the effect of magnetic shear increases the value of $k_\perp$ sufficiently that this coupling is weak. The degree to which the value of $k_\perp\delta_e$ changes is largely determined by the first term on the right-hand side of Eq. (58), because, from Fig. 4(a), it can be seen that the derivative, $q'(r)$, is very small at the flux surface being examined. The behavior illustrated by Fig. 13 indicates that resonator modes can clearly exist for cold plasma conditions.

Next, the effects of finite ion temperature in the presence of magnetic shear are considered. Figure 13 is the analog of Fig. 12, but at a slightly lower frequency, $\omega = 1.005\omega_{ii}$, and with ion temperature included. For this case, $m = 4$ is chosen for both displays. The ion temperature at this flux surface is $T_i = 27.8$ keV, and corresponds to the solid line in both panels. For the dashed line, the ion temperature is artificially lowered to $T_i = 7.0$ keV, to provide a comparison. It is found that for temperatures below $T_i = 2.8$ keV the cold plasma result shown in Fig. 14 is recovered, but it is not shown. The top panel, Fig. 13(a), illustrates coupling to an ion-Bernstein wave (IBW), as evidenced by the lobes that appear in the display. The appearance of these lobes causes an increase of both the length of the resonator and of the area under the curves shown in this panel. When magnetic shear and FLR effects are included, the quantization condition, Eq. (24), causes the value of the eigenfrequency to decrease for a given n. The bottom panel, Fig. 13(b), illustrates the corresponding increase in the value of $k_\perp$. The variations in $k_\perp$ have two

significant consequences. First, the damping of the wave increases with increased $k_\perp$. Second, the instability driven by the alpha particles can be tuned and detuned depending on the local value of $k_\perp$. Such a spatial variation is expected to reduce the amplification factors reported in Sec. IV. However, many different modes can be amplified at each poloidal position, and subsequently can carry the energy to other locations.

VI. CONCLUSIONS

The present investigation of an ion-ion hybrid Alfvén resonator for D-T burning plasma conditions expected in the ITER device is motivated by well-established experimental observations. In a large, linear magnetic confinement device, operating with plasmas having two ion species, shear Alfvén waves have been measured to reflect at the position where the wave frequency equals the value of the ion-ion frequency [8]. In the same device, but operating with a magnetic well configuration, this reflection property has been used to demonstrate the formation of resonator modes [14]. In a research tokamak [9], waves launched by a small antenna in a hydrogen-deuterium plasma have been observed to experience guided propagation along field lines, and to exhibit strong poloidal localization determined by the value of the ion-ion hybrid frequency. The present analytical and modeling study has explored how the challenging environment of burning plasmas modify the trapping properties of such modes.

A detailed study of the kinetic dispersion relation for shear Alfvén waves, including coupling to the compressional mode, has been made for the relevant burning plasma conditions. It is identified that the high ion temperatures introduce a variation of the reflection points of the resonator modes with perpendicular wave number. A one-dimensional WKB analysis based on the kinetic dispersion relation has been used to determine the eigenfrequencies of trapped modes. It is found that ion cyclotron damping limits the possible resonator modes to a narrow bandwidth (on the order of 500 kHz) above the local ion-ion hybrid frequency on the outboard side of a given magnetic surface. Within this bandwidth several weakly damped resonator modes can be found. The modes experience strong poloidal localization (ranging from 10 to 50 degrees) about the midplane. The spatial amplification of resonator modes driven by energetic, fusion-born alpha particles has been considered. The alpha particles are modeled using a ring distribution, which is relevant to the post-birth phase of the alpha particles before collisional relaxation occurs. It is determined that such a ring distribution can effectively couple energy into shear Alfvén modes, resulting in roughly three e-foldings of amplification in one pass through the resonator.

A preliminary assessment of the effects caused by magnetic shear has been made. The primary effect is the increase in the value of the perpendicular wave number as the shear Alfvén wave propagates along the resonator. Under cold

plasma conditions, this effect prevents energy transfer to the compressional mode, and, in a sense, provides for a more robust resonator. But it is found that such behavior pertains to ion temperatures below 2.8 keV. For larger ion temperatures the magnetic shear causes the Alfvén wave to couple to an ion-Bernstein mode. This in turn lengthens the resonator and reduces the reflection efficiency. The increase in the value of $k_\perp$ also can increase the damping along the propagation path, although this effect may be offset somewhat by the decrease of $k_{||}$ as the wave approaches the cut-off point. The instability drive by the alpha particles can also be affected by the variations in $k_\perp$. This can lead to spatial tuning and detuning of the wave resonance with the alpha particle population, possibly reducing the amplification factors reported.

In summary, the presence of an ion-ion hybrid Alfvén resonator has unique signatures that may be sampled in future burning plasma experiments. The results of this investigation provide clear guidelines for comprehensive studies of related phenomena (e.g., plasma rotation, alpha channeling) that should be based on advanced computational techniques that expand on the present frontier RF codes such as AORSA [29] and TORIC [30].

ACKNOWLEDGEMENTS

The work at UCLA is sponsored by DOE grant DE-SC0007791. W. A. F. is a Lawrence scholar and his work was performed under the auspices of the U.S. Department of Energy by Lawrence Livermore National Laboratory under Contract DE-AC52-07NA27344.

REFERENCES

[1] S. J. Buchsbaum, Phys. Fluids **3**, 418 (1960).

[2] R. L. Smith and N. Brice, J. Geophys. Res. **69**, 5029, doi:10.1029/JZ069i023p05029 (1964).

[3] J. Jacquinot, B. D. McVey, and J. E. Scharer, Phys. Rev. Lett. **39**, 88 (1977).

[4] F. W. Perkins, Nucl. Fusion **17**, 1197 (1977).

[5] R. Majeski, C. K. Phillips, and J. R. Wilson, Phys. Rev. Lett. **73**, 2204 (1994).

[6] E. F. Jaeger, L. A. Berry, E. F. D'Azevedo, R. F. Barrett, S. D. Ahern, D. W. Swain, D. B. Batchelor, R. W. Harvey, J. R. Myra, D. A. D'Ippolito, c. K. Phillips, E. Valeo, D. N. Smithe, P. T. Bonoli, J. C. Wright, and M. Choi, Phys. Plasmas **15**, 072513 (2008).

[7] C. Castaldo and A. Cardinali, Phys. Plasmas **17**, 072513 (2010).

[8] S. T. Vincena, G. J. Morales, and J. E. Maggs, Phys. Plasmas **17**, 52106 (2010).

[9] G. G. Borg and R. C. Cross, Plasma Phys. Contr. F. **29**, 681-696 (1987).

[10] T. Intrator, M. Vukovic, A. Elfimov, P. H. Probert, and G. Winz, Phys. Plasmas **3**, 1054 (1996).

[11] A. V. Guglielmi, A. S. Potapov, and C. T. Russell, Pis'ma Zh. Eksp. Teor. **72**, 432 (2000); JETP Lett. **72**, 298-300 (2000).

[12] V. E. Moiseenko and E. Tennfors, Plasma Phys. and Control. Fusion **38**, 2133 (1996).

[13] S. T. Vincena, W. A. Farmer, J. E. Maggs, and G. J. Morales, Geophys. Res. Lett. **38**, L11101, doi:10.1029/2011GL047399 (2011).

[14] S. T. Vincena, W. A. Farmer, J. E. Maggs, and G. J. Morales, Phys. Plasmas **20**, 012111 (2013).

[15] W. A. Farmer and G. J. Morales, Phys. Plasmas **20**, 082132 (2013).

[16] W. A. Farmer, G. J. Morales, S. T. Vincena, and J. E. Maggs. Proceedings of the 39th European Conference on Plasma Physics and 16th Int. Congress on Plasma Physics, Stockholm, 2012, edited by S. Ratynskaya, L. Blomberg, and A. Fasoli (European Physical Society, Stockholm, 2012), p. P.4064.

[17] N. J. Fisch and J.-M. Rax, Phys. Rev. Lett. **4**, 612 (1992).

[18] D. S. Darrow, R. Majeski, N. J. Fisch, R. F. Heeter, H. W. Herrmann, M. C. Herrmann, M. C. Zarnstorff, and S. J. Zweben, Nucl. Fusion **4**, 509 (1996).

[19] D. S. Darrow, S. J. Zweben, S. Batha, R. V. Budny, C. E. Bush, Z. Chang, C. Z. Cheng, H. H. Duong, J. Fang, N. J. Fisch, R. Fischer, E. D. Fredrickson, G. Y. Fu, R. F. Heeter, W. W. Heidbrink, H. W. Herrmann, M. C. Herrmann, K. Hill, E. F. Jaeger, R. James, R. Majeski, S. S. Medley, M. Murakami, M. Petrov, C. K. Phillips, M. H. Redi, E. Ruskov, D. A. Spong, E. J. Strait, G. Taylor, R. B. White, J. R. Wilson, K.-L. Wong, and M. C. Zarnstorff, Phys. Plasmas **3**, 1875 (1996).

[20] D. S. Clark and N. J. Fisch, Phys. Plasmas **7**, 2923 (2000).

[21] C. N. Lashmore-Davies and D. A. Russell, Phys. Plasmas **4**, 369 (1997).

[22] Y. Lin, J. E. Rice, S. J. Wukitch, M. J. Greenwald, A. E. Hubbard, A. Ince-Cushman, L. Lin, E. S. Marmar, M. Porkolab, M. L. Reinke, N. Tsujii, and J. C. Wright, Phys. Plasmas **16**, 056102 (2009).

[23] N. Tsujii, M. Porkolab, P. T. Bonoli, Y. Lin, J. C. Wright, S. J. Wukitch, E. F. Jaeger, D. L. Green, and R. W. Harvey, Phys. Plasmas **19**, 082508 (2012).

[24] C. Gormezano, A. C. C. Sips, T. C. Luce, S. Ide, A. Becoulet, X. Litaudon, A. Isayama, J. Hobirk, M. R. Wade, T. Oikawa, R. Prater, A. Zvonkov, B. Lloyd, T. Suzuki, E. Barbato, P. Bonoli, C. K. Phillips, V. Vdovin, E. Joffrin, T. Casper, J. Ferron, D. Mazon, D. Moreau, R. Bundy, C. Kessel, A. Fukuyama, N. Hayashi, F. Imbeaux, M. Murakami, A. R. Polevoi, and H. E. St John, Nucl. Fusion **47**, S285 (2007).

[25] M. Brambilla, *Kinetic Theory of Plasma Waves: Homogeneous Plasmas* (Oxford University Press, New York, 1998).

[26] J. A. C. Weideman, Siam J. Numer. Anal. **31**, 1497 (1994).

[27] R. V. Budny, Nucl. Fusion **42**, 1383 (2002).

[28] M. A. Beer, S. C. Cowley, and G. W. Hammett, Phys. Plasmas **2**, 2687 (1995).

[29] E. F. Jaeger, L. A. Berry, E. F. D'Azevedo, R. F. Barrett, S. D. Ahern, D. W. Swain, D. B. Batchelor, R. W. Harvey, J. R. Myra, D. A. D'Ippolito, C. K. Phillips, E. Valeo, D. N. Smithe, P. T. Bonoli, J. C. Wright, and M. Choi, Phys. Plasmas **15**, 072513 (2008).

[30] J. C. Wright, P. T. Bonoli, M. Brambilla, F. Meo, E. D'Azevedo, D. B. Batchelor, E. F. Jaeger, L. A. Berry, C. K. Phillips, and A. Pletzer, Phys. Plasmas **11**, 2473 (2004).

Figure Captions

Figures

Fig. 1. (Color online) Kinetic dispersion relation of the shear Alfvén wave for burning plasmas expected in ITER. Magnetic field strength is 53 kG, electron density is 5.9×10^{13} cm^{-3}, electron temperature is 31.1 keV, with equal concentrations of deuterium and tritium with temperatures of $T_D = T_T = 27.8$ keV. Horizontal axes are the frequency scaled to the tritium gyrofrequency, ω/Ω_T. (a) Contour plot of real part of scaled parallel wave number, $k_{||}v_A/\Omega_T$, with scaled perpendicular wave number, $k_\perp\delta_e$, on the vertical axis. Coupling to compressional wave is seen at small $k_\perp\delta_e$. Cutoff frequency approaches ion-ion hybrid frequency, $\omega_{ii}/\Omega_T = 1.22$, at intermediate values of $k_\perp\delta_e$ and due to FLR effects, bends towards the tritium cyclotron frequency. (b) Line-cuts of panel (a). The cuts are made at $k_\perp\delta_e = 0.045$ (solid), 0.145 (dashed), 0.245 (dashed-dotted), and 0.345 (solid with dotted

markers). Downward shift of cutoff frequency with increasing $k_\perp \delta_e$ is clearly seen. (c) Arguments of plasma dispersion functions illustrating relative importance of electron Landau and ion-cyclotron damping. Line-styles correspond to same values of $k_\perp \delta_e$ as in panel (b). Black curves, labeled "electrons", correspond to electron Landau damping for which $\zeta = \left|\omega/\sqrt{2}k_{||}\bar{v}_e\right|$. Red and blue curves, labeled "Deuterium" and "Tritium", correspond to tritium and deuterium cyclotron damping, respectively, for which $\zeta = \left|(\omega - \Omega_i)/\sqrt{2}k_{||}\bar{v}_e\right|$. Cyclotron damping is dominant over most of the frequency range except near the cutoff.

Fig. 2. (Color online) Imaginary part of parallel wave number for parameters used in Fig. 1. Horizontal axes are the scaled frequency, ω/Ω_T. (a) Contour plot of imaginary part of $k_{||}v_A/\Omega_T$ with scaled perpendicular wave number, $k_\perp \delta_e$, on the vertical axis. (b) Line-cuts of panel (a). Line-styles correspond to same values of $k_\perp \delta_e$ in Fig. 1(b).

Fig. 3. (Color online) Effective damping experienced in one wavelength, $\eta = 2\pi\ \mathrm{Im}(k_{||})/\mathrm{Re}(k_{||})$, for parameters used in Fig. 1. Horizontal axes are the scaled frequency, ω/Ω_T. (a) Contour plot of η with scaled perpendicular wave number, $k_\perp \delta_e$, on the vertical axis. The value $\eta = 1$, is shown by the white contour. Regions to the right of this contour are heavily damped, and regions to the left illustrate where candidate resonator modes exist. (b) Line-cuts of panel (a). Line-styles correspond to same values of $k_\perp \delta_e$ in Fig. 1(b).

Fig. 4. Radial profiles of plasma parameters used in analysis. Profiles determined from Fig. 41(c) and (d) of Ref. 24, adapted to a cylindrical approximation for the tokamak geometry. The horizontal axis corresponds to radius from the magnetic axis. (a) Radial dependence of electron density and safety factor. The left vertical axis corresponds to electron density (solid curve). The right vertical axis corresponds to the safety factor (dashed curve). (b)Radial dependence of electron and ion temperatures. The left vertical axis corresponds to temperature in keV. The electron and ion temperatures correspond to the solid and dashed lines, respectively. The temperatures of deuterium and tritium are assumed to be equal.

Fig. 5. (Color online). Radial dependence of possible resonator parameters. Horizontal axes correspond to radius from magnetic axis. Electron density, safety factor, and electron and ion temperatures are given in Fig. 4. Magnetic field strength is given by Eq. (19) with $B_0 = 53$ kG and $R = 621$ cm; perpendicular wavelength is $\lambda_\perp = 10$ cm, corresponding to $k_\perp \delta_e = 0.043$ at the magnetic axis. (a) Radial dependence of relevant frequencies. Vertical axis corresponds to frequency in MHz. Bottom black curve corresponds to the fundamental eigenfrequency in the resonator, ω_0. Red curve corresponds to frequency of modes having $Q = 20$, $\omega_{Q=20}$. The slanted green line, labeled ω_{Max}, corresponds to the cut-off frequency on the inboard side; waves in the blank region to its left are not trapped. This frequency terminates when the deuterium cyclotron frequency on the inboard side, represented by the top orange curve labeled, $\Omega_{\mathrm{D,inboard}}$, because of heavy cyclotron damping. The blue hatched region, labeled "Damped", corresponds to strongly

damped modes with $Q < 20$. (b) Vertical axis corresponds to the number of long-lived modes with $Q > 20$.

Fig. 6. Dependence of the Quality factor, Q, on resonator mode number. The horizontal axis corresponds to the mode number, and the vertical axis, to Q. The plasma parameters used for the solid curve are the same as those given in Fig. 5 evaluated at $r = 50$ cm; the electron temperature is $T_e = 31.1$ keV, and the scaled perpendicular wave number, $k_\perp \delta_e = 0.0433$. The dashed curve uses the same parameters, except that the electron and ion temperatures are decreased proportionally, so that $T_e = 8.39$ keV. The dash-dotted curve, similarly, uses the same parameters as the solid curve, except that $k_\perp \delta_e = 0.1433$. In reality, modes with Q>100 are essentially undamped by wave-particle interactions and would be limited by some other mechanism.

Fig. 7. Number of long-lived modes as a function of scaled perpendicular wave number. The horizontal axis corresponds to the scaled perpendicular wave number, $k_\perp \delta_e$, and the vertical axis, to the number of modes with $Q > 20$, $n_{Q>20}$. The rapid decrease is due to increased cyclotron damping as $k_\perp$ increases.

Fig. 8. Poloidal extent of the trapped modes. Horizontal axis corresponds to the radius, r, and the vertical axis, to the size of the well measured in poloidal angle, $\Delta\theta$. The reflection points occur at $\theta_0 = \pm \Delta\theta/2$. The solid curve corresponds to the fundamental mode, and the dashed curve, to a mode for which $Q = 20$. The poloidal extent of long-lived modes falls between the two curves. The increase towards the magnetic axis is a geometrical effect, while the increase in the dashed curve towards the edge is due to rapid decreases in plasma density and temperature.

Fig. 9. Imaginary part of $k_{||}$ due to a ring-distribution of alpha particles for different values of $k_\perp$. Calculation performed for a homogeneous plasma with parameters corresponding to Fig. 4 at position, $r = 50$ cm on the outboard side. This corresponds to magnetic field, $B_0 = 49.1$ kG, electron density, $n_e = 5.9\times10^{13}$ cm^{-3}, electron temperature, $T_e = 31.1$ keV, and ion temperatures, $T_D = T_T = 27.8$ keV. Equal concentrations of deuterium and tritium are assumed. The alpha-particle distribution is described by Eq. (39), with temperatures, $T_{\perp\alpha} = 2$ MeV and $T_{||\alpha} = 1.5$ MeV, and density, $n_\alpha = 0.01 n_e$. On the horizontal axis is the scaled frequency, and on the vertical axis, the imaginary part of the parallel wave number, Im $k_{||}$. The solid and dashed curves correspond to $\lambda_\perp = 9$ and 5 cm, respectively. Instability drive is present when Im $k_{||}$ is negative, for the solid curve, and is caused by a negative value of P_1 in Eq. (40).

Fig. 10. Imaginary part of $k_{||}$ for different resonator modes within one well. The background plasma parameters are the same as in Fig. 5 evaluated at $r = 50$ cm, and the alpha distribution parameters are those used in Fig. 11. The horizontal axis corresponds to distance along a field line, and the vertical axis, to the imaginary part of $k_{||}$. The dashed, solid, and dashed-dotted curves correspond to the mode numbers,

$n = 7, 17,$ and 27 with amplification factors, $A = 2.6, 3.1,$ and 2.6, respectively. The mode with largest amplification is $n = 17$. For higher mode numbers, damping towards the center limits the growth, and at lower mode numbers, the well decreases in length, limiting total amplification.

Fig. 11. Amplification factors at different radii. The background plasma parameters are the same as in Fig. 5 evaluated at $r = 50$ cm, and the alpha distribution parameters are those used in Fig. 11. On the horizontal axis is the frequency range of the amplified modes in MHz, and on the vertical axis, the amplification factor. The individual curves correspond to $r = 25, 50, 100,$ and 150 cm, and are labeled accordingly. The continuous decrease in the frequency band results in a spread of several MHz over which the resonator can be amplified across the plasma. The increase in A towards the magnetic axis is a geometrical effect, which lengthens the well. The increase towards the edge is due to the colder background plasma. In reality, this increase will be offset by a decrease in alpha particle density towards the edge.

Fig. 12. Effects of magnetic shear on resonator modes in a cold plasma. The background plasma parameters are as in Fig. 5 evaluated at $r = 50$ cm, except that the plasma temperature is artificially set to zero. The frequency of the wave is $\omega = 1.01\omega_{ii}$, where ω_{ii} is given by Eq. (1), with the cyclotron frequencies evaluated at the outboard side. The horizontal axes correspond to distance along a field line, s. The solid, dashed, and dash-dotted lines correspond to $m = 4, 8,$ and 12. (a) Dependence of $k_{||}^2$. (b) Dependence of $k_\perp \delta_e$. Both panels show that the reflection point is largely independent of $k_\perp$. As m increases, the magnetic shear more effectively changes the value of $k_\perp$, resulting in a distorted profile for $k_{||}^2$.

Fig. 13. Effects of magnetic shear on resonator modes in a hot plasma. The background plasma parameters are as given in Fig. 5, evaluated at $r = 50$ cm, with $m = 4$ and the ion temperatures set to 27.8 keV and 7.0 keV for the solid and dashed lines, respectively. The frequency of the wave is $\omega = 1.005\omega_{ii}$. (a) Dependence of $k_{||}^2$. (b) Dependence of $k_\perp \delta_e$. The difference in cut-off points between the solid and dashed lines is attributed to the reduction in the Larmor radius. If the temperature is further decreased, the result approaches the cold plasma behavior shown in Fig. 12.

Figures

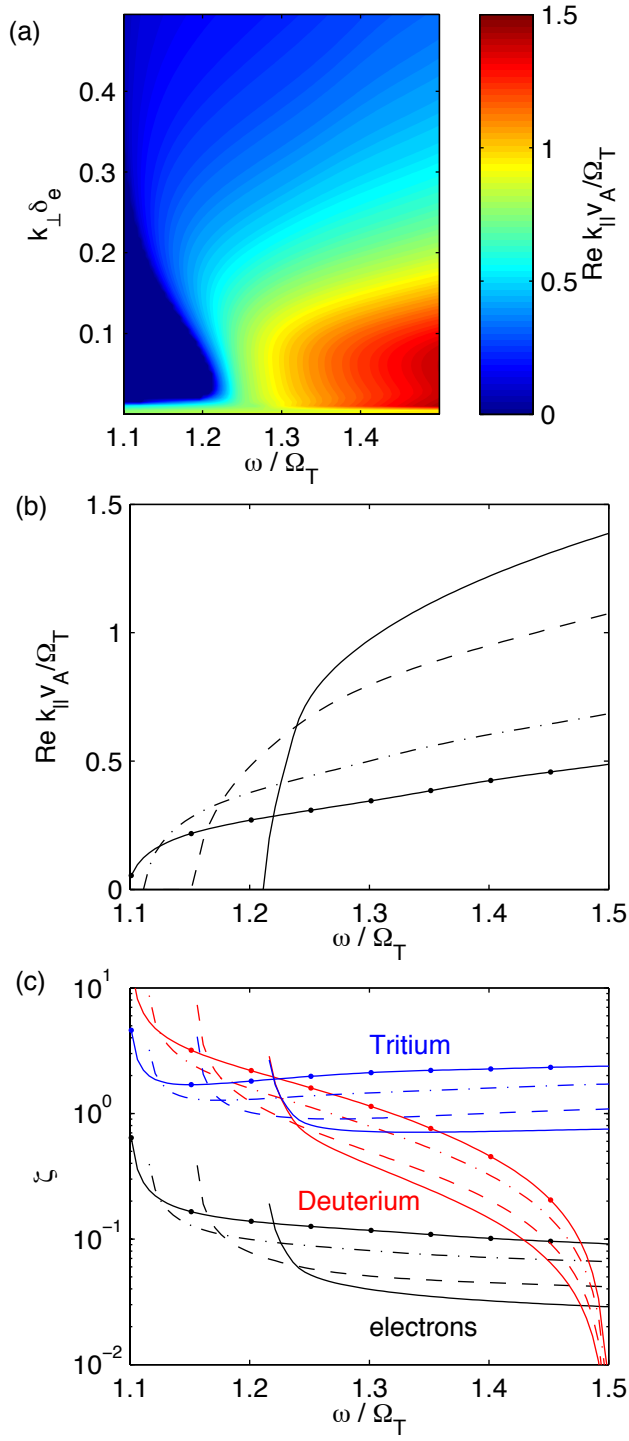
(a)
0.4
0.3
0.2
0.1
$k_\perp \delta_e$
1.1
1.2
1.3
1.4
ω / Ω_T
1.5
1
0.5
0
Re $k_{||} v_A / \Omega_T$
(b)
1.5
1
0.5
0
Re $k_{||} v_A / \Omega_T$
1.1
1.2
1.3
1.4
1.5
ω / Ω_T
(c)
10^1
10^0
10^{-1}
10^{-2}
ζ
Tritium
Deuterium
electrons
1.1
1.2
1.3
1.4
1.5
ω / Ω_T

Figure 1

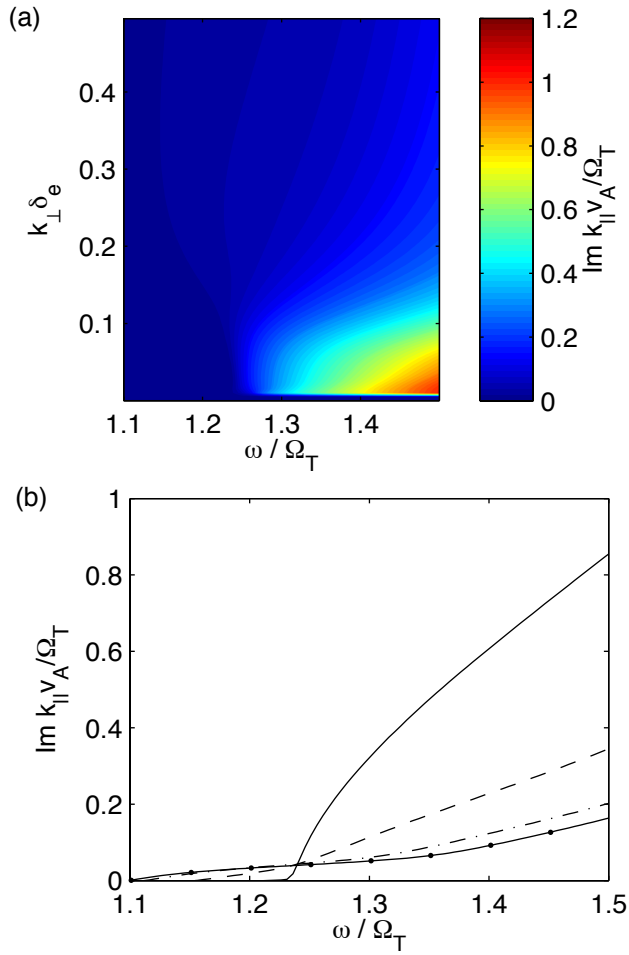
(a)
0.4
0.3
0.2
0.1
$k_\perp \delta_e$
1.1
1.2
1.3
1.4
ω / Ω_T
1.2
1
0.8
0.6
0.4
0.2
0
$\mathrm{Im}\, k_{\parallel} v_A / \Omega_T$
(b)
1
0.8
0.6
0.4
0.2
0
$\mathrm{Im}\, k_{\parallel} v_A / \Omega_T$
1.1
1.2
1.3
1.4
1.5
ω / Ω_T

Figure 2

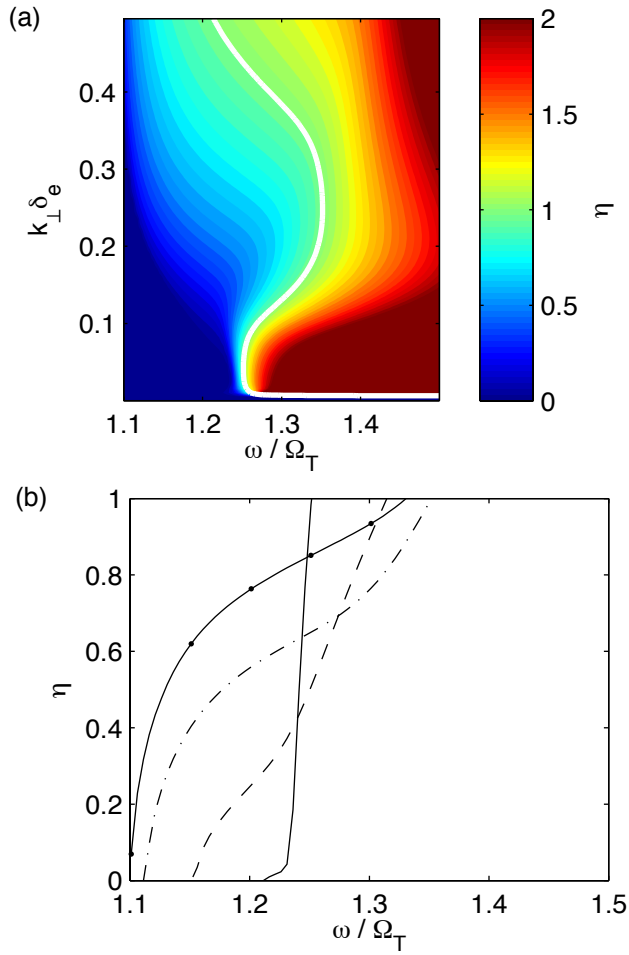
(a)
0.4
0.3
0.2
0.1
$k_\perp \delta_e$
1.1
1.2
1.3
1.4
ω / Ω_T
2
1.5
1
0.5
0
η
(b)
1
0.8
0.6
0.4
0.2
0
η
1.1
1.2
1.3
1.4
1.5
ω / Ω_T

Figure 3

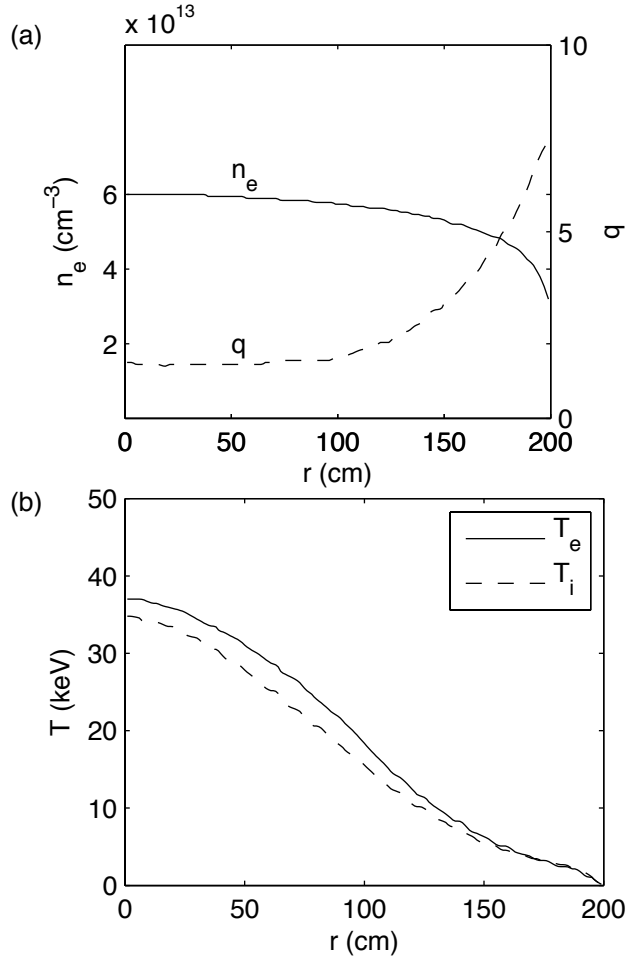

Figure 4

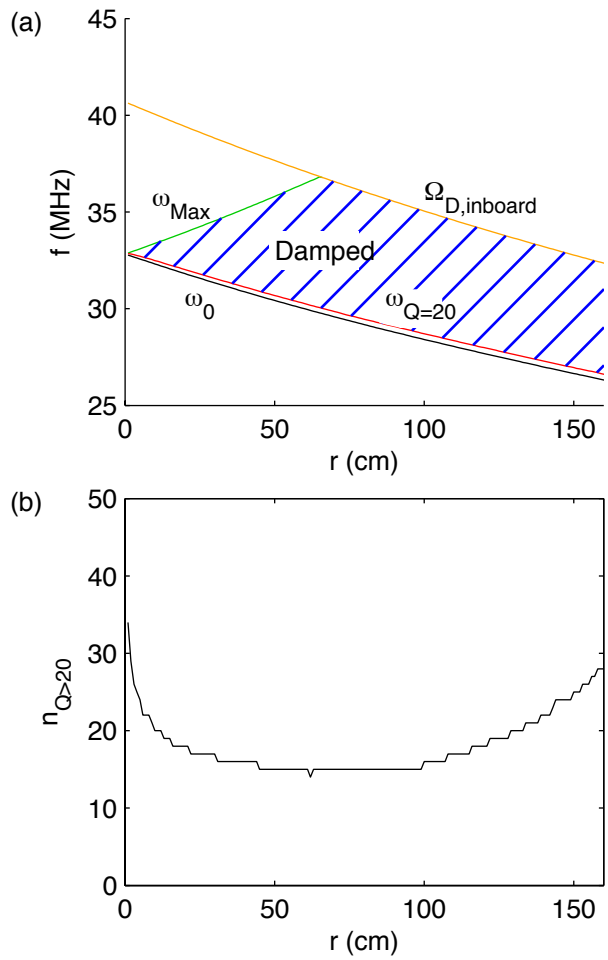

Figure 5

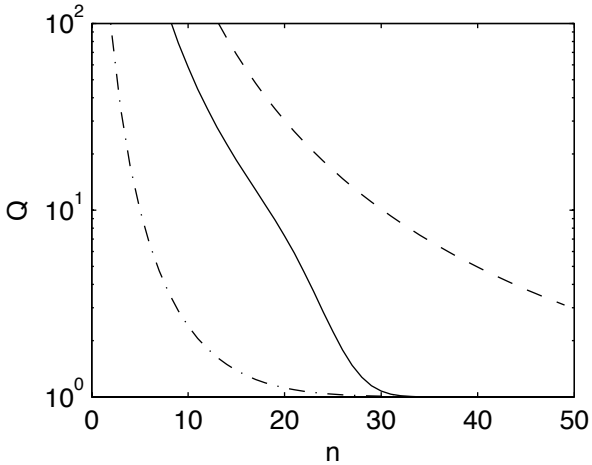

Figure 6

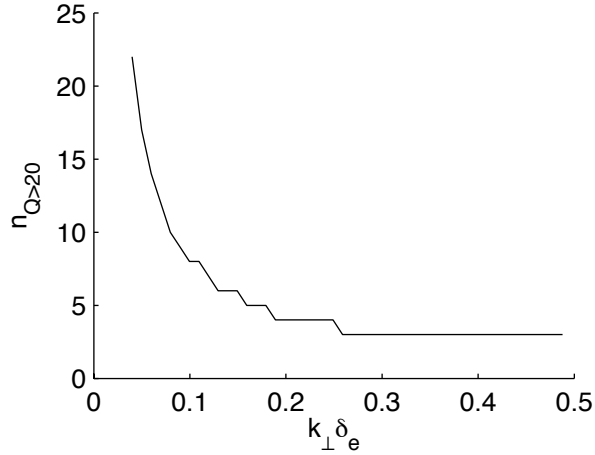

Figure 7

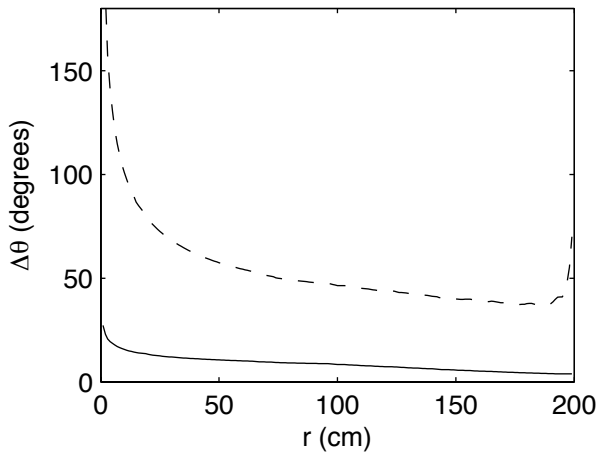

Figure 8

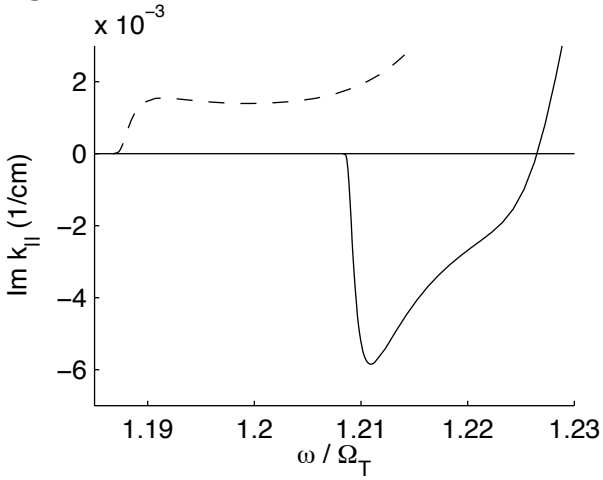

Figure 9

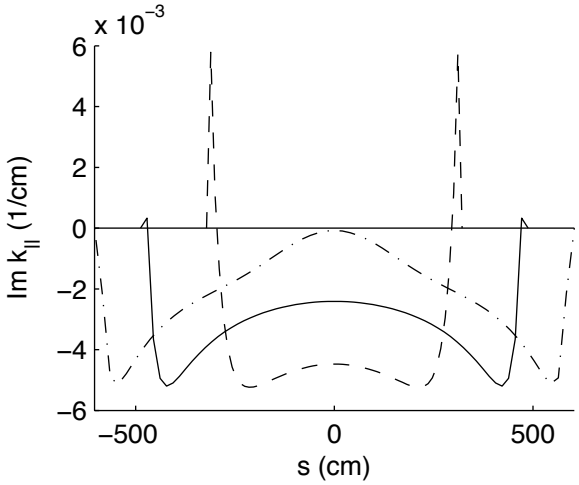

Figure 10

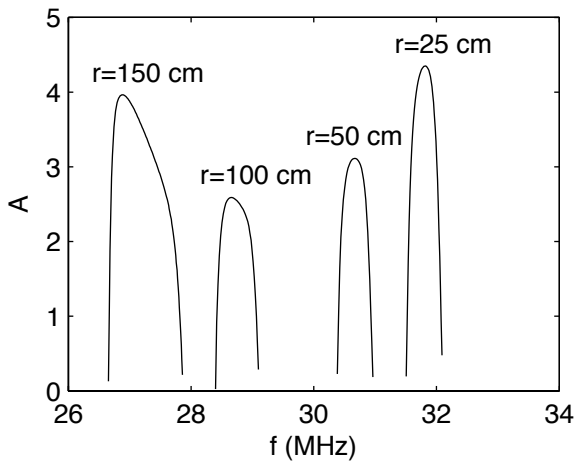

Figure 11

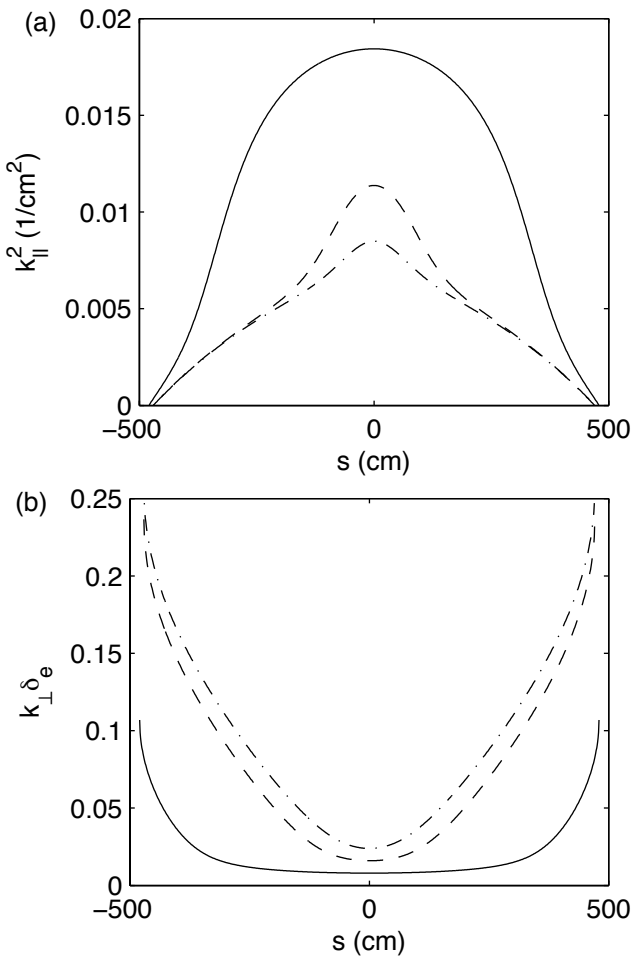
(a)
0.02
0.015
0.01
0.005
0
$k_{\parallel}^2$ (1/cm^2)
−500
0
500
s (cm)
(b)
0.25
0.2
0.15
0.1
0.05
0
$k_{\perp}\delta_e$
−500
0
500
s (cm)

Figure 12

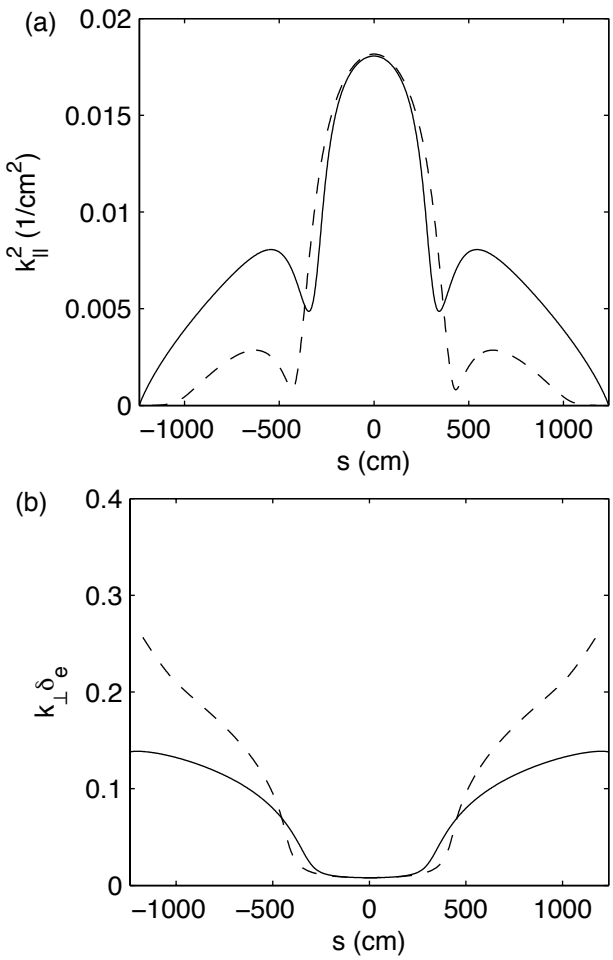
(a)
0.02
0.015
0.01
0.005
0
$k_{\parallel}^2$ (1/cm^2)
−1000
−500
0
500
1000
s (cm)
(b)
0.4
0.3
0.2
0.1
0
$k_{\perp}\delta_e$
−1000
−500
0
500
1000
s (cm)

Figure 13